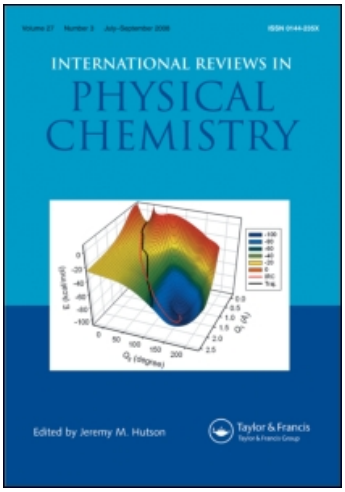

International Reviews in Physical Chemistry
Publication details, including instructions for authors and subscription information:
http://www.informaworld.com/smpp/title~content=t713724383

Probing reactive potential energy surfaces by vibrational activation of H_2-OH entrance channel complexes

Martyn D. Wheeler[a]; David T. Anderson[a]; Marsha I. Lester[a]
[a] Department of Chemistry, University of Pennsylvania, Philadelphia, PA, USA

Online publication date: 26 November 2010

INT. REVIEWS IN PHYSICAL CHEMISTRY, 2000, VOL. 19, NO. 4, 501–529

Probing reactive potential energy surfaces by vibrational activation of H_2–OH entrance channel complexes

MARTYN D. WHEELER†, DAVID T. ANDERSON‡
and MARSHA I. LESTER§
Department of Chemistry, University of Pennsylvania,
Philadelphia, PA 19104-6323, USA

This review article presents an overview of recent experimental and theoretical studies of reactant complexes composed of OH and H_2 that have been stabilized in the entrance channel to the OH + H_2 → H_2O + H hydrogen abstraction reaction. The first part focuses on infrared and stimulated Raman spectroscopic measurements of H_2–OH complexes with particular emphasis on characterizing the bound states supported by the intermolecular well in the entrance channel. The experimental vibrational spectra are compared with first principles quantum calculations to assign the observed intermolecular levels and quantify the degree of body-fixed orientation achievable within the reactant complex. The second part explores the lifetime and inelastic scattering dynamics of vibrationally activated H_2–OH upon OH and H_2 stretching excitation. The half-collision dynamics, which sample a restricted range of initial orientations in the H_2–OH complex, provide complementary information to full-collision studies of reactive and inelastic scattering dynamics of OH + H_2, and direct comparisons are made between the various studies. The article concludes by summarizing some of the remaining questions about the decay dynamics of vibrationally activated H_2–OH entrance channel complexes that require further experimental and theoretical work.

1. Introduction

Hydrogen atom abstraction from molecules by the free radicals F, OH, NH_2 and CH_3 forms perhaps the simplest class of elementary reactions, and as such are often considered as the centrepiece for models of chemical reactivity. Over the past decade, there have been tremendous advances in experimental and theoretical investigations of the dynamics of hydrogen atom abstraction reactions, especially the simplest ones: F + H_2 → HF + H, Cl + CH_4 → HCl + CH_3 and OH + H_2 → H_2O + H [1–6]. These studies strive to gain a precise understanding of the forces that govern the rates and mechanisms of the elementary chemical processes by characterizing the underlying potential energy surface (PES) [7, 8]. Much of this activity has focused on the region about the transition state [9–12], the saddle point that separates reagents and products, as this region clearly plays a critical role in the reaction dynamics.

As our understanding of molecular reaction dynamics has matured, it has become recognized that features of the PES far removed from the transition state region, such as shallow wells in the reactant and product valleys, can play a decisive role in

† Present address: Department of Chemistry, University of Leicester, University Road, Leicester, LE1 7RH, UK.
‡ Present address: Department of Chemistry, University of Wyoming, Laramie, Wyoming 82071-3838, USA.
§ Email: milester@sas.upenn.edu

International Reviews in Physical Chemistry ISSN 0144-235X print/ISSN 1366-591X online
http://www.tandf.co.uk/journals

the outcome of encounters between reactive species [13–15]. These shallow minima on neutral surfaces arise from long-range attractive forces between reactants due to van der Waals interactions, such as dispersion and electrostatic interactions. At low collision energies these long-range forces can exert a strong influence over the collision dynamics by orienting the reactants relative to one another as they approach the transition state region. The anisotropic long-range forces can guide the reagents to a favourable mutual orientation for reaction or steer the molecular orientation away from a configuration suitable for reaction. A striking example is provided by Liu and co-workers' recent investigation of the Cl + HD reaction at low collision energies [14]. Exact quantum scattering calculations attribute the strong preference observed for DCl products to a T-shaped attractive well in the entrance channel that deflects a portion of the reactive flux away from the collinear transition state configuration.

While this example illustrates that long-range forces can influence chemical reactions, few experiments have directly probed the weak intermolecular interactions between reactive species. Experimental investigations of intermolecular interactions have generally concentrated on closed-shell systems that are non-reactive [16, 17], and those that have considered open-shell radical species have mainly been concerned with the interaction with an inert gas partner [18–20]. Recent experiments have begun to examine the intermolecular interactions between reactive partners, such as H_2 + OH, CH_4 + OH, H_2 + CN and Cl + HCl, in the entrance channel to hydrogen abstraction reactions [21–34]. The H_2–OH system in its ground electronic state is the focus of this review article.

The OH + H_2 → H_2O + H reaction has emerged as a benchmark for the theoretical and experimental investigation of four-atom reaction dynamics [7, 35]. This reaction represents the most elementary chemical process involving hydrogen abstraction by OH radicals, and is also important in combustion and interstellar chemistry [36, 37]. A schematic illustration of the reaction pathway is given in figure 1. The key features to note along the reaction coordinate are an early barrier (2130 cm^{-1}) with a transition state structure beginning to resemble the H_2O product and an exit channel with a large release of energy (5180 cm^{-1}) to the H_2O + H products [6]. The experimental activation energy for the reaction is found to be ~1380 cm^{-1} [39], demonstrating that quantum mechanical tunnelling through the barrier plays an important role at low collision energies. Additionally, the entrance channel contains a shallow well (−188 cm^{-1}) in a T-shaped OH–H_2 configuration that arises from the long-range attractive interactions between the reactants [38]. This shallow well is the starting point for the experimental work described in this review article.

The PES most widely used to describe the OH + H_2 reaction, developed by Schatz and Elgersma from *ab initio* calculations by Walch and Dunning, is tailored to reproduce the transition state region [40, 41]. This surface has been used extensively in theoretical investigations of the reaction dynamics ranging from classical trajectory studies [41–43] to exact full dimensionality quantum scattering [44–46], although it is known to suffer from some serious flaws especially in the entrance channel to reaction. Newly fitted surfaces are now emerging that encompass more *ab initio* points [6, 47, 48]. In addition, *ab initio* calculations by Miller, Clary, Kleisch and Werner (MCKW) [38] as well as others [49, 50] have concentrated on developing potentials that describe the long-range behaviour in the OH + H_2 entrance channel accurately. These non-reactive potentials have been used to simulate the results of

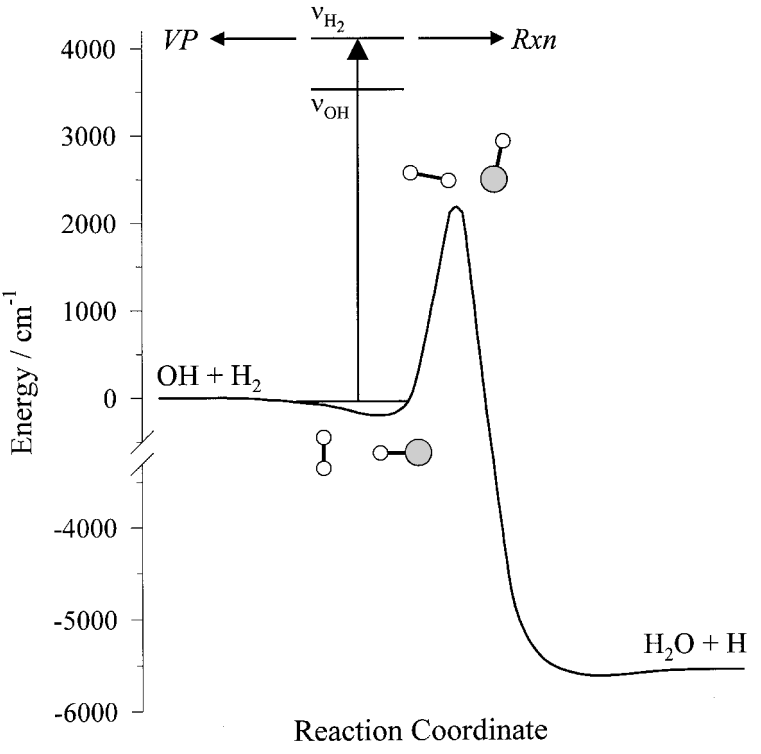

Figure 1. Schematic reaction pathway for the ground state OH + H_2 → H_2O + H hydrogen abstraction reaction. The reactants are stabilized in a weakly bound complex within a shallow well in the entrance channel to reaction. Vibrational excitation of the H_2 or OH stretching mode in the H_2–OH complexes provides sufficient energy to surmount the barrier to reaction (Rxn) or, alternatively, to rupture the weak intermolecular bond via vibrational predissociation (VP). The barrier height and structure are obtained from *ab initio* calculations of the transition state [6], while the minimum energy configuration and well depth in the entrance channel are taken from separate *ab initio* calculations of the long-range interaction between the reactants [38]. The ground state binding energy for H_2–OH has been determined in previous electronic spectroscopy measurements [22].

state-to-state inelastic scattering experiments [38, 51–55] and to predict the infrared spectrum associated with weakly bound complexes formed from the OH and H_2 reactants [38, 56]. Recently, there has been some effort to combine the reactive and non-reactive potentials with the goal of obtaining an improved global PES for the OH + H_2 system [57].

The reaction of OH with H_2 has been the focus of numerous laboratory investigations, with nearly every modern experimental technique for studying gas phase dynamics having been applied to this system. These include detailed kinetic rate measurements over a wide range of temperatures [39], state selective laser excitation of reactants and/or products [58, 59], molecular beam scattering studies [5, 6], and electron photodetachment of the H_3O^- negative ion [12]. The OH (v = 0) + H_2 (v = 0) → H_2O + H reaction has been found to be relatively slow at room temperature [39], approximately five orders of magnitude slower than the gas kinetic collision rate. Vibrational activation of the OH partner with one or two quanta of

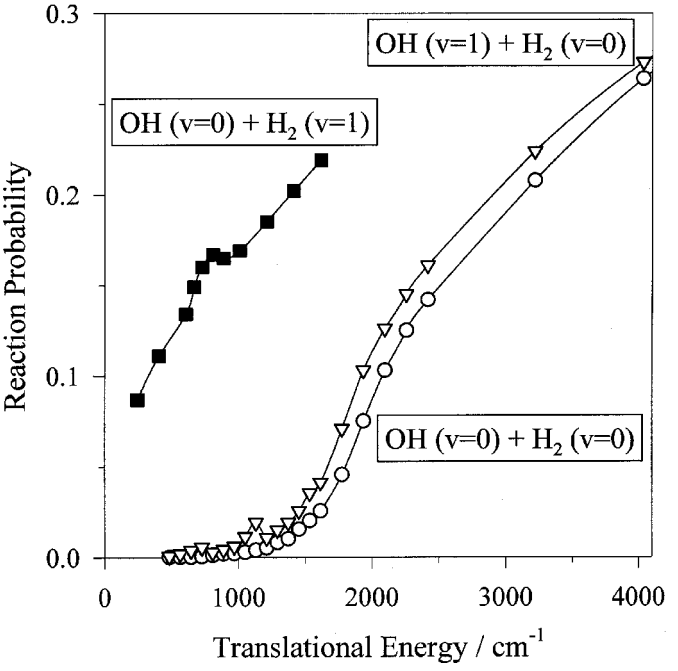

Figure 2. Theoretically predicted reaction probability for H_2 ($v = 0, 1$) + OH ($v = 0, 1$) as a function of translational energy, computed in time-dependent wavepacket calculations by Zhang and Zhang [44, 64, 65]. The reaction probability is essentially unchanged upon vibrational excitation of OH as compared to the ground state reaction, with a threshold that is commensurate with the effective barrier to reaction. For vibrationally excited H_2, the reaction probability is significantly enhanced and the threshold for reaction drops to nearly zero. These calculations illustrate the concept that H_2 is a reactive bond and OH is a spectator bond in the OH + H_2 → H_2O + H hydrogen abstraction reaction.

stretching excitation has been shown to enhance the rate coefficient by less than 50% [60]. This observation has been interpreted in terms of the OH bond playing only a spectator role in the reaction process. In contrast, kinetic studies of the reaction of vibrationally excited H_2 with OH radicals have revealed a 120- to 155-fold increase in the rate coefficient over the ground state reaction [61, 62]. Vibrational excitation of H_2 has a more direct influence on the rate of reaction, as this is the bond that will ultimately be cleaved during the reaction.

Dynamical calculations also predict a significant mode selectivity in the rate of reaction [42, 44, 63–67]. The time-dependent quantum wavepacket calculations of Zhang and Zhang are reproduced in figure 2 to illustrate this effect [44, 64, 65]. The reaction probability for ground state reagents exhibits a translational energy threshold at $\sim$1200 cm^{-1} that reflects the effective barrier to reaction, with increasing reaction probability at higher kinetic energies. The reaction probability and translational energy threshold are essentially unchanged upon vibrational excitation of OH, even though $\sim$3600 cm^{-1} of vibrational energy has been added to the OH reagent. Vibrational activation of H_2, however, significantly enhances the reaction probability at a given translational energy. In addition, the energetic threshold for reaction drops to nearly zero [44], effectively removing the barrier to reaction for H_2 ($v = 1$) with OH ($v = 0$).

We have been pursuing a new approach for investigating the OH + $H_2 \rightarrow H + H_2O$ reaction by stabilizing H_2–OH complexes in the entrance channel to reaction. The H_2–OH complex was first observed via electronic spectroscopy utilizing the strong OH $A\ ^2\Sigma^+$–$X\ ^2\Pi$ electronic transition by Loomis and co-workers in 1995 [21–23]. These studies revealed the surprising result that the reactants to this low-barrier, exothermic hydrogen exchange reaction could be trapped in the shallow intermolecular well in the entrance channel to reaction. Since then, our experiments have focused on vibrational activation of H_2–OH entrance channel complexes in order to explore the spectroscopy and dynamics of H_2–OH in its ground electronic state [24–29].

Vibrational spectroscopy of H_2–OH provides detailed information on the shape of the OH + H_2 PES in the entrance channel to reaction. These spectroscopic measurements, however, are unlike those of typical van der Waals complexes, because infrared or stimulated Raman excitation of the high frequency intramolecular modes ($\nu_{H_2} \approx 4155\,cm^{-1}$ and $\nu_{OH} \approx 3568\,cm^{-1}$) [68, 69] of H_2–OH supply more than sufficient energy to initiate reaction (Rxn) between the OH and H_2 partners. Alternatively, the vibrational excitation of H_2–OH may result in vibrational predissociation (VP), an inelastic scattering event that breaks apart the H_2–OH complex and regenerates the OH + H_2 reactants. These decay channels are illustrated in figure 1. The vibrationally activated H_2–OH complex can decay by vibrational predissociation or reaction, depending on the coupling between the initially prepared H_2–OH state and the continuum of states that evolve into reactants or products. These unimolecular decay processes should exhibit a high degree of mode selectivity, as found previously in bimolecular collision studies of OH + H_2, as well as stereo-selectivity, due to the restricted range of initial orientations sampled in the H_2–OH complex.

This review brings together recent experimental work performed in this laboratory [24–29] and related theoretical studies [25, 29, 38, 56] on vibrational excitation of H_2–OH entrance channel complexes. Section 2 describes the experimental procedures for the generation and subsequent vibrational excitation of H_2–OH. The following sections describe the vibrational spectroscopy (section 3), the bound intermolecular states (section 4), and the dynamics (section 5) associated with activation of the OH and H_2 modes in the H_2–OH complex. The final section discusses the likelihood of reaction within the H_2–OH complex (section 6) before concluding (section 7).

2. Experimental method

This section presents a concise summary of the procedure for generating and probing H_2–OH entrance channel complexes; the reader is referred to previous publications for a more detailed description [26–28]. Hydroxyl radicals are produced in a pulsed supersonic expansion by the 193 nm photolysis of nitric acid in a 30% normal-H_2–He carrier gas at a backing pressure of ~10 atm. The photolysis occurs prior to expansion within a quartz capillary attached to the pulsed solenoid valve assembly. The photolytically generated OH can react with H_2 present in the carrier gas or, alternatively, can be cooled below the threshold to reaction in the ensuing supersonic expansion. The H_2–OH entrance channel complexes are formed in the low temperature environment of the free jet expansion. To optimize the formation of H_2–OH and enhance the cooling of the OH (translational, rotational, and to some extent vibrational), the temperature of the pulsed valve assembly is lowered to ~0°C with a Peltier cooling chip.

2.1. *Vibrational excitation*

The H_2–OH entrance channel complexes are vibrationally excited ~1.5 cm downstream of the photolysis position in the collision free regime of the expansion. Vibrational activation is accomplished using one of two experimental procedures: either two quanta of vibrational excitation is deposited into the OH partner using pulsed infrared excitation or one quantum of vibration is placed into the H_2 partner by means of pulsed stimulated Raman excitation. The vibrationally activated complexes are denoted as H_2–OH ($v_{OH} = 2$) or H_2–OH ($v_{H_2} = 1$), respectively.

An injection-seeded Nd:YAG (Continuum Powerlite 9010) pumped BBO optical parametric oscillator (OPO) (Continuum Sunlite) is used to produce infrared light in the OH overtone region near 1.4 μm. The 10 Hz repetition rate IR pump pulses are 12 mJ per pulse with a frequency bandwidth of 0.12 cm^{-1}. Alternatively, stimulated Raman excitation (SRE) was effected using two visible lasers pulses, denoted PUMP and STOKES, that were both generated by an injection-seeded Nd:YAG pumped dye laser system (Continuum ND6000). A portion of the 532 nm second-harmonic output of the Nd:YAG was used as the PUMP laser. The STOKES dye laser (operating at around 683 nm) was tuned such that the difference in frequency between the PUMP and STOKES laser was in the vicinity of the fundamental vibrational transition of H_2 at 4155 cm^{-1}. The PUMP and STOKES laser pulses were copropagated into the vacuum chamber with parallel polarization. The SRE laser source was also operated at a 10 Hz repetition rate, with each of the two laser pulses on the order of 100 mJ per pulse and a combined frequency bandwidth of 0.06 cm^{-1}.

2.2. *Pump–probe detection schemes*

Detection of vibrationally activated H_2–OH has been achieved using three different pump–probe schemes which are illustrated in figure 3. Subsequent to the IR (or SRE) vibrational excitation process outlined above, a UV probe laser monitors one of the following: depletion of the ground state population of the H_2–OH complex (fluorescence depletion, FD), enhancement in the population of the vibrationally excited state of the complex (fluorescence enhancement, FE), or appearance of OH fragments produced by the fragmentation of the vibrationally activated complex (action spectroscopy). The UV probe laser operates at a 20 Hz repetition rate, twice that of the IR (or SRE) pump laser.

Both the fluorescence depletion and enhancement schemes utilize previously identified electronic transitions associated with the H_2–OH complex [21, 22]. In the FD method, the UV probe laser (Quantel YG-580 and TDL 60) is fixed on an electronic transition arising from the ground intermolecular state supported by the OH X $^2\Pi$ ($v = 0$) + H_2 ($v = 0$) potential and terminating on bound levels correlating with the OH A $^2\Sigma^+$ ($v = 1$) + H_2 ($v = 0$) asymptote, resulting in a laser-induced fluorescence (LIF) signal. As the IR or SRE pump frequency is scanned over vibrational transitions of the complex, population is removed from the ground state of H_2–OH resulting in a reduction, or depletion, of the UV probe LIF signal. In the FE mode, the UV probe laser (Quantel YG-580 and TDL 60 or Lambda Physik EMG 201 MSC and FL 2002) is fixed on a transition originating from intermolecular levels supported by the vibrationally excited OH X $^2\Pi$ ($v = 2$) + H_2 ($v = 0$) potential and terminating on the same electronically excited levels as in the FD method. In this case, a LIF signal is observed only when the IR pump laser is

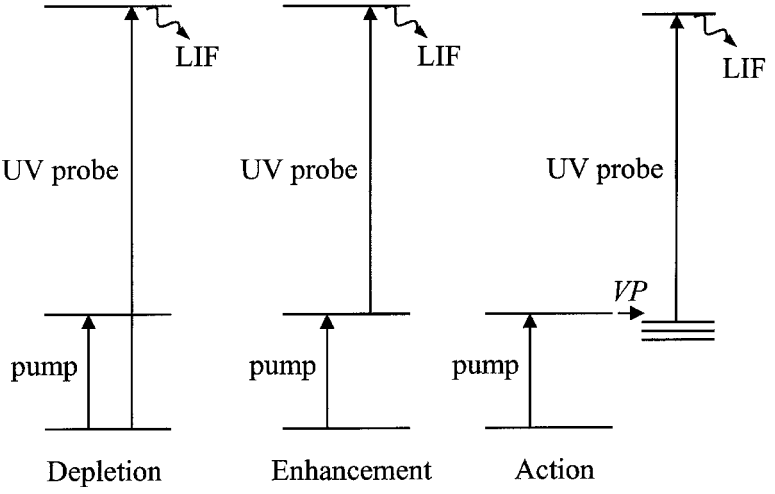

Figure 3. Illustration of the three pump–probe schemes employed to investigate the vibrational spectroscopy and decay dynamics of H_2–OH. In each case, the pump laser promotes H_2–OH to a vibrationally excited state. In depletion, the UV probe laser monitors the H_2–OH ground state population via laser-induced fluorescence (LIF), with vibrational excitation of H_2–OH detected as a decrease in LIF signal. In enhancement, the UV probe laser detects population transferred to vibrationally excited levels of H_2–OH by LIF. In action, the UV probe laser detects OH fragments from vibrational predissociation (VP) of H_2–OH by LIF.

resonant with an OH overtone transition of the H_2–OH complex, since there is no initial population of the vibrationally excited complex in the supersonic expansion.

The action spectroscopy method relies on the vibrational predissociation of H_2–OH (v_{OH} = 2) or (v_{H_2} = 1) complexes to produce OH fragments, which are subsequently detected by the UV probe laser (Lambda Physik EMG 201 MSC and FL 2002). Specifically, the UV probe laser is fixed on a particular rovibronic transition in the OH A–X (0,1) band at 346 nm [70], since excitation of both the OH overtone and H_2 fundamental vibration of H_2–OH complexes is expected to lead to OH (v = 1) fragments via vibrational predissociation (see section 5). Therefore, whenever the IR or SRE pump laser is resonant with a rovibrational transition of the complex, a LIF signal is observed due to the production of OH (v = 1) fragments.

The relative merits and drawbacks associated with the FD and FE methods have been discussed previously [26, 71, 72]. Briefly, the FD method is the closest to direct absorption spectroscopy and therefore provides the most general approach to studying the vibrational spectroscopy of H_2–OH complexes. However, FD is inherently a non-zero background technique. In order to observe the vibrational transitions, the IR or SRE pump laser source must induce depletions in the UV LIF signal that are greater than the baseline fluctuations in the H_2–OH LIF signal. By contrast, the FE and action spectroscopy methods are zero background: the LIF signal is present only when the IR or SRE pump laser is resonant with transitions of the H_2–OH complex. These two methods provide higher sensitivity detection schemes than FD, but require *a priori* knowledge of either the approximate frequencies of the vibrational transitions or the open product state channels from the dissociation dynamics of the vibrationally activated complex. Action spectroscopy offers the most

versatile method for studying H_2–OH complexes since it allows the decay dynamics of vibrationally activated H_2–OH to be probed in the time and frequency domains.

Time domain experiments enable direct measurement of the decay rate of the vibrationally activated H_2–OH complex. These measurements are performed by stepping the relative time delay between the IR (or SRE) pump and UV probe laser pulses, with the IR (or SRE) pump laser frequency fixed on a particular rovibrational transition of the H_2–OH complex and the UV probe laser frequency set to detect a specific OH (v = 1) fragment quantum state. Frequency domain measurements yield the relative populations of the nascent OH X $^2\Pi$ (v = 1) product rotational states, providing insights into the mechanism for vibrational predissociation of H_2–OH (v_{OH} = 2) or (v_{H_2} = 1). These latter experiments are achieved by scanning the probe laser frequency over various OH A–X lines [70] with the pump laser set on a rovibrational transition of H_2–OH at a fixed time delay.

In all three of the methods described above, the UV probe laser was counter-propagated along the axis established by the IR or SRE lasers. The lasers were synchronized such that an IR or SRE laser pulse was present for every other UV laser pulse. The UV probe LIF was collected by $f/1$ optics (lenses and spherical mirror), passed through spectral filters to discriminate against laser scatter and a spatial filter to define the viewing region, and detected with a photomultiplier tube. The LIF signal was preamplified, integrated and transferred to a computer for further processing. On alternating pulses, the LIF signal arising from the UV laser *only* or that resulting from the *combination* of the IR+UV or SRE+UV lasers was collected. The difference between the LIF signal obtained with and without vibrational excitation was recorded and averaged at each time or frequency step.

3. Vibrational spectroscopy

The infrared and stimulated Raman spectra of H_2–OH have been obtained using the pump–probe detection schemes described in the previous section. The vibrational spectroscopy provides quantitative information on the intramolecular vibrational frequencies, intermolecular transition frequencies, and rotational band structure including parity splittings for the H_2–OH complex. The intramolecular vibrational frequencies reveal the changes in the covalent bonds upon complexation. The energies of the intermolecular states in H_2–OH can be directly related to the angular and radial characteristics of the potential in the entrance channel to reaction.

3.1. *OH overtone excitation*

The rotationally resolved infrared overtone spectrum of H_2–OH is illustrated in figure 4 over the wavenumber range 6964–7024 cm^{-1} [24, 26]. This particular spectrum was recorded via the fluorescence enhancement scheme by fixing the UV probe laser on an H_2–OH feature in the OH A–X (1,2) region at 351 nm and scanning the IR pump laser. The position of the OH monomer $Q(3/2)$ overtone transition at 6971.3 cm^{-1} is indicated on the abscissa for comparison [69]. All of the lines in the spectrum are attributed to H_2–OH. OH monomer transitions do not appear in the experimental spectrum due to the double-resonance condition of the FE technique.

The infrared overtone spectrum of H_2–OH can be divided into two spectral regions. The first region consists of the closely spaced cluster of lines centred at around 6972 cm^{-1} and is attributed to rovibrational transitions of the pure OH stretching overtone of the H_2–OH complex with no intermolecular excitation [24, 26]. The

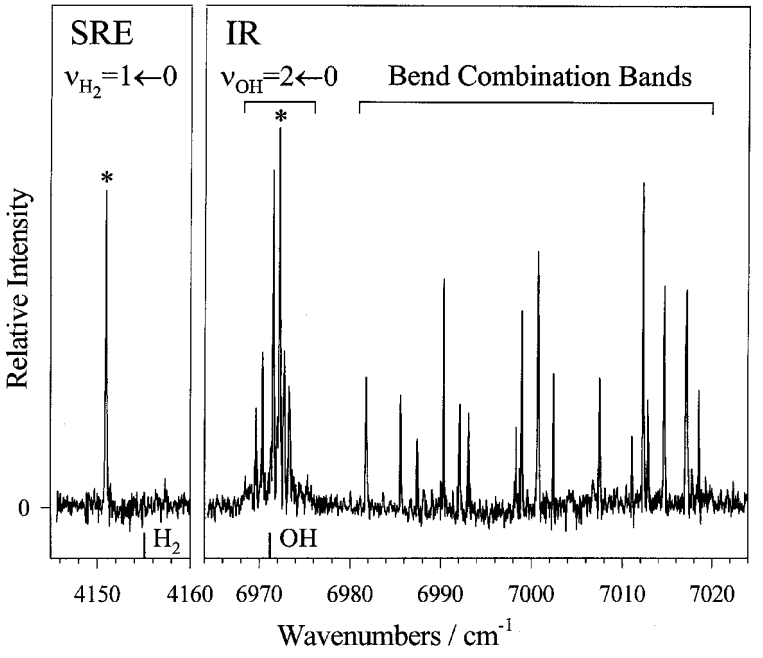

Figure 4. Left panel: stimulated Raman excitation (SRE) spectrum of the H_2 fundamental (v_{H_2} = 1 ← 0) in *o*-H_2–OH recorded via the SRE-UV action method (adapted from [28]). The single feature observed is an unresolved *Q*-branch at 4151.5 cm^{-1}. Right panel: infrared (IR) spectrum of *o*-H_2–OH recorded via the IR–UV enhancement method (adapted from [26]). Rovibrational transitions of the pure OH overtone band (v_{OH} = 2 ← 0) are centred at 6971.9 cm^{-1} (origin) and transitions towards higher energy are bend combination bands involving the simultaneous excitation of OH overtone and intermolecular bending vibrations. The positions of the corresponding monomer transitions are shown for comparison. The asterisks indicate the IR and SRE transitions that are pumped in dynamical studies.

basis of this assignment follows from the fact that this is the most intense band observed in the spectrum, the spectral frequency of the band is consistent with an OH monomer overtone origin, and that no other features were observed to lower frequency than 6968 cm^{-1}. The second region encompasses approximately 20 rovibrational transitions to higher energy of the pure overtone band ($\geqslant$6980 cm^{-1}) that extend almost to the OH X $^2\Pi$ (v = 2) + H_2 dissociation threshold (determined in separate experiments to be D_0 = 54 cm^{-1}) [22]. These additional spectral features are attributed to bend combination band transitions involving simultaneous excitation of the OH stretching overtone and intermolecular bend motions of the H_2 and/ or OH monomers (more on intermolecular bend states in section 4).

The H_2–OH complex can exist in two possible forms with the OH monomer interacting with either *para*-H_2 (*p*-H_2) or *ortho*-H_2 (*o*-H_2), each of which will possess a distinct intermolecular energy level pattern and infrared spectrum [38, 56]. Detailed analysis of the experimental infrared spectrum has revealed that only complexes containing *o*-H_2 contribute to the infrared spectrum shown in figure 4 [26]. The *o*-H_2–OH complexes are expected to be the dominant species present in the supersonic expansion for two reasons. First, *o*-H_2 (j_{H_2} = 1) is favoured over *p*-H_2 (j_{H_2} = 0) in an ideal supersonic expansion of normal-H_2 by a 3:1 ratio according to nuclear spin

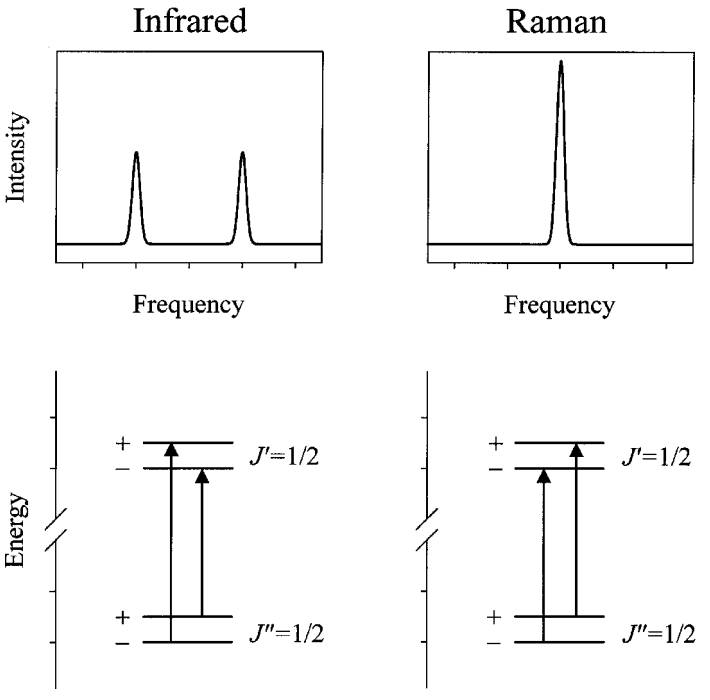

Figure 5. The appearance of the infrared and Raman spectra of o-H_2–OH are considerably different due in part to different parity selection rules. The change in parity required for infrared transitions ($v_{OH} = 2 \leftarrow 0$) causes Q-branch transitions to be split apart by the sum of the parity splitting in the ground and excited rovibrational states. In contrast, no change in parity for Q-branch transitions in Raman spectra ($v_{H_2} = 1 \leftarrow 0$) results in overlapping transitions, even though the parity splitting in the ground and excited rovibrational states is large.

statistics. Second, theoretical calculations predict that o-H_2–OH complexes will be more strongly bound than p-H_2–OH (47 cm^{-1} versus 28 cm^{-1}, respectively) [38], due to the more anisotropic interaction between OH and o-H_2 ($j_{H_2} = 1$). This difference in binding energy leads to preferential complexation, thereby further enriching the *ortho*: *para* ratio in the H_2–OH complex. Similar observations have been reported for the H_2–HF complex [73, 74].

The rotational structure of the pure OH overtone band is dominated by a strong central Q-branch. Each line in the band corresponds to a rovibrational transition originating from a specific total angular momentum J and parity p level in the ground state of o-H_2–OH. The pure overtone band has been assigned as a $K = 1/2 \leftarrow 1/2$ transition of o-H_2–OH based on a detailed comparison with *ab initio* theory [24, 26]. Here, K is the magnitude of the body-fixed projection of the total angular momentum J along the intermolecular axis R. Analysis of the experimental spectrum indicates that each of the rovibrational transitions in the Q-branch is split into a doublet corresponding to transitions between states of the same total angular momentum but opposite parity. The two most intense lines in the pure overtone band are assigned as $Q(1/2)$ lines. The frequency difference between the two parity components of the $Q(1/2)$ transition is equal to the *sum* of the parity splittings for the $J = 1/2$ rotor levels in the ground intermolecular states

with $v_{OH} = 0$ and $v_{OH} = 2$. This is illustrated in figure 5 for the $Q(1/2)$ transition using the dipole allowed selection rules for H_2–OH, namely $\Delta J = 0$ and $p'' \neq p'$ [75]. The midpoint between the two $Q(1/2)$ lines gives the band origin for the pure overtone transition of o-H_2–OH at 6971.9 cm^{-1}, shifted 0.6 cm^{-1} to higher energy of the corresponding OH monomer transition (position indicated in figure 4) [24]. This small spectral shift corresponds to a mere 80 ppm change in the OH vibrational overtone frequency upon complexation with o-H_2 and demonstrates that the OH intramolecular vibration is only weakly coupled to the intermolecular degrees of freedom in H_2–OH.

The combination band transitions have also been assigned based on a comparison with the rovibrational spectrum predicted from *ab initio* theory [26]. For example, the first combination band feature observed at 6981.8 cm^{-1} is assigned to overlapping parity components of the $Q(1/2)$ rovibrational transitions that terminate on an excited $K = 1/2$ bending state. This excited bend state is assigned as a $K = 1/2$ state because the calculated intermolecular energy, 10.1 cm^{-1}, agrees remarkably well with the experimentally measured intermolecular energy, 9.9 cm^{-1}, determined from the difference between the peak frequency and the H_2–OH pure overtone origin [26]. The calculations also indicate that the parity splitting in the excited $K = 1/2$ bending level is approximately equal in magnitude to that in the ground intermolecular state, but with opposite ordering of the parity levels. As a result, the two parity components of the $Q(1/2)$ transitions are predicted to overlap within 0.1 cm^{-1}, consistent with the single unresolved peak that is observed. The agreement between experiment and theory for these lowest two bands, as well as higher frequency transitions [26], indicates that the MCKW potential provides a good description of o-H_2–OH in its ground and excited bend states.

3.2. *H_2 fundamental excitation*

The stimulated Raman spectrum of H_2–OH is illustrated in figure 4 over the wavenumber range 4145–4160 cm^{-1} [28]. This spectrum was recorded via action spectroscopy by detecting OH ($v = 1$) fragments produced from the vibrational predissociation of H_2–OH ($v_{H_2} = 1$). The example spectrum shown in figure 4 was obtained by fixing the UV probe laser on the OH A–X (0,1) $Q_1(9/2)$ rovibronic transition and scanning the STOKES laser. This particular OH probe transition was empirically selected based on the magnitude of the LIF signal when the SRE lasers were resonant with the H_2–OH transition. A single peak is observed in the stimulated Raman spectrum centred at 4151.5 cm^{-1}, which is attributed to vibrational excitation of the fundamental H_2 stretch in o-H_2–OH. For comparison, the $Q_1(1)$ monomer transition of the o-H_2 fundamental occurs at 4155.3 cm^{-1} (position indicated in figure 4) [68]. Again, note that H_2 monomer lines do not appear in the experimental spectrum due to the double-resonance condition of the action spectroscopy technique.

The fact that only a single feature is observed in the SRE spectrum provides further evidence that under these experimental conditions the o-H_2–OH complex is the dominant species in the jet. The peak in the SRE spectrum is ascribed to the Q-branch of the o-H_2–OH pure H_2 fundamental, since this rotational branch typically dominates Raman spectra [76]. In order to provide support for this assignment, the intensity dependence of the o-H_2–OH feature was investigated as a function of the relative polarization of the stimulated Raman PUMP and STOKES lasers. No signal was observed in a crossed polarization arrangement. From this observation, we infer

that the *o*-H_2–OH feature observed with parallel polarization is a *Q*-branch and that the Raman activity for this stimulated Raman transition is derived mainly from the isotropic part of the molecular polarizability [76]. This same term is primarily responsible for the Raman activity of the H_2 monomer [77].

No other spectral features have been observed within a 100 cm^{-1} range of this single feature. The absence of any bend combination bands in the SRE spectrum suggests that either transitions to excited intermolecular states of *o*-H_2–OH have small Raman cross-sections or, alternatively, that combination band transitions are extensively homogeneously broadened causing the transition strength to be spread over a broad spectral range and making them difficult to detect using narrow bandwidth lasers. Felker *et al.* have suggested that intermolecular vibrations involving large-amplitude librational motion of one of the monomers are expected to have significant Raman transition strengths [78]. Since the monomers undergo nearly free internal rotation in *o*-H_2–OH (see section 4), the absence of combination band transitions in the SRE spectrum is surprising and may signal that a rapid decay process is occurring.

The *Q*-branch feature in the SRE spectrum is not split into doublets like the *Q*-branch in the infrared spectrum because of the different selection rules, namely $\Delta J = 0$ and $p'' = p'$, for Raman transitions [75]. Therefore, if the parity splitting does not change appreciably (in either sign or magnitude) upon vibrational excitation of H_2, then the two parity components of the $Q(1/2)$ transition should overlap in the Raman spectrum, as illustrated in figure 5 and observed experimentally. In SRE, the frequency difference between the two $Q(1/2)$ transitions is a measure of the *difference* in the parity splitting of the $J = 1/2$ rotor level of *o*-H_2–OH with $v_{H_2} = 0$ and $v_{H_2} = 1$. The breadth of the *Q*-branch feature in the SRE spectrum is greater than the laser resolution (0.06 cm^{-1}) and may be due to a combination of factors: unresolved rotational structure within the *Q*-branch, power broadening and/or homogeneous lifetime broadening.

The pure H_2 fundamental is shifted 3.8 cm^{-1} to lower energy of the $Q_1(1)$ transition of free *o*-H_2, a much larger shift than observed for the OH vibration. The decrease in the H_2 vibrational frequency upon complexation can be interpreted as a weakening and, therefore, lengthening of the H_2 bond in the *o*-H_2–OH complex. This may be a consequence of coupling to the intermolecular degrees of freedom and/or the OH + H_2 reaction coordinate. An analogous lengthening of the H_2 bond occurs upon approach to the transition state for the OH + H_2 reaction [40, 47, 66], where the H–H distance is approximately 10% longer than the expectation value of the bond length for the H_2 ($v = 1$) molecule (0.79 Å) [79].

4. Characterizing the intermolecular states of H_2–OH

This section provides an overview of complementary theoretical calculations on the H_2–OH system by Clary and co-workers, including *ab initio* potentials and bound state calculations [38, 56]. It also extends the previous theoretical studies by transforming the bound state wave functions to the body-fixed frame, which enables the angular properties of the wave function to be visualized. The angular probability distributions illustrate the well-defined relative orientation of the OH and H_2 reactants within the H_2–OH complex for specific intermolecular states.

4.1. *Potential energy surface*

For collinear approach of OH and H_2, a single $^2\Pi$ electronic state correlates with the OH X $^2\Pi$ + H_2 X $^1\Sigma_g^+$ asymptote (neglecting the spin–orbit interaction). At nonlinear geometries, the cylindrical degeneracy of this $^2\Pi$ state is lifted resulting in two potential surfaces. For planar configurations (C_s symmetry), these two surfaces can be characterized as having $^2A'$ or $^2A''$ symmetry depending on whether the half-filled $p\pi$-orbital of OH lies in-plane or out-of-plane, respectively. At long-range (3–10 Å) these two surfaces are close in energy, while at short range (1–3 Å) they can be widely separated, and this energy difference depends strongly on the relative orientation of the OH and H_2 moieties. Only the A′ surface correlates adiabatically with the H + H_2O reaction products and, as a result, theoretical studies of the reaction include only the A′ surface [40].

The nuclear dynamics of the H_2–OH entrance channel complex sample both the A′ and A″ surfaces. Therefore, potentials that include both the reactive (A′) and non-reactive (A″) surfaces are needed to calculate the bound states and infrared spectrum of H_2–OH. In 1994, Miller *et al.* calculated *ab initio* points for both the A′ and A″ surfaces as a function of the four intermolecular coordinates using the coupled electron pair approximation [38]. These calculations rigorously treat both the A′ and A″ adiabatic surfaces in the entrance channel, but do not consider reactive regions of the potential (the OH and H_2 bond lengths are held fixed). The *ab initio* data were used to construct a four-dimensional interaction potential (MCKW), which has since been utilized for inelastic scattering and bound state calculations [38].

For computational convenience in the dynamical calculations, the two potential surfaces are expanded as average $V_{AVG} = \frac{1}{2}(V_{A'} + V_{A''})$ and difference $V_{DIF} = \frac{1}{2}(V_{A'} - V_{A''})$ potentials. The global minimum on the average surface ($V_{AVG} = -188.1\,cm^{-1}$) is located in a T-shaped OH–H_2 geometry ($\theta_{OH} = 0°$, $\theta_{H_2} = 90°$) with intermolecular separation $R = 3.22$ Å, where the A″ surface is $\sim 18\,cm^{-1}$ lower in energy than the A′ surface. The T-shaped minimum is derived predominantly from electrostatic interactions (dipole–quadrupole and quadrupole–quadrupole) [38]. A local minimum ($V_{AVG} = -168.0\,cm^{-1}$) is found at a shorter $R = 2.90$ Å with an L-shaped configuration ($\theta_{OH} = 102°$, $\theta_{H_2} = 29°$) [26], which resembles the transition state structure [6]. The polar angles θ_{OH} and θ_{H_2} are defined as the angle between the diatom bond axis and the intermolecular axis.

The bound state energies evaluated on the MCKW PES have been used to calculate transition frequencies [38], which can be directly compared with the infrared and stimulated Raman spectra presented in the last section. From this type of comparison, the MCKW PES has been shown to be qualitatively correct [24, 26]. Therefore, the MCKW potential will be used as a model of the interaction potential between the OH and H_2 reactants in the entrance channel.

4.2. *Correlation diagram*

A correlation diagram for the bound states of *o*-H_2–OH based on the MCKW potential is presented in figure 6 [38]. The intermolecular states of *o*-H_2–OH with $\pm$ parity *p* are derived from the lowest rotor levels of the monomers, *o*-H_2 ($j_{H_2} = 1$) and OH ($j_{OH} = 3/2$, $l = 3/2$). A detailed analysis has revealed that the wave functions for the bound states of *o*-H_2–OH can be constructed primarily (>90%) from terms that involve only these lowest rotational states of the monomers [80].

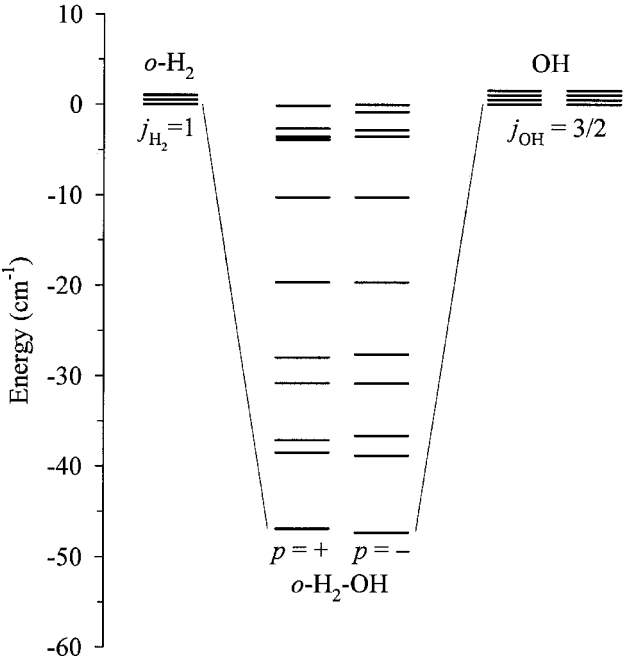

Figure 6. Intermolecular energy level diagram showing the bound states of o-H_2–OH with parity p that correlate with the lowest rotor levels of the o-H_2 (j_{H_2} = 1) and OH (j_{OH} = 3/2, ! = 3/2) monomers. The degeneracy of each monomer rotor level is illustrated, including lambda-doublet components for OH, as these degeneracies are lifted in the complex. The ground intermolecular state of o-H_2–OH is bound by ~47 cm^{-1} based on the MCKW *ab initio* potential [38].

The weak intermolecular potential does not mix higher rotational state character into the H_2 or OH angular wave functions as a result of the large rotational spacings in H_2 (B = 59.334 cm^{-1}) and OH (B = 18.55 cm^{-1}) [69, 79]. Thus, the o-H_2 and OH diatoms undergo nearly free rotation in o-H_2–OH.

Nevertheless, the presence of the nearby o-H_2 partner lifts the orientational degeneracy of the OH j_{OH} = 3/2 rotor through a first-order Stark effect, giving rise to $2j_{OH}$ + 1 = 4 angular states with different body-fixed projections. Similarly, the presence of OH will lift the orientational degeneracy of the o-H_2 j_{H_2} = 1 rotor, resulting in three angular states. Together, the interaction of o-H_2 (j_{H_2} = 1) with OH (j_{OH} = 3/2) can yield 4 × 3 = 12 intermolecular bend states of both + and − total parity [56]. Intermolecular stretching excitation can then be built on each of these bend states, although the lowest eight bound states shown in figure 6 are intermolecular bend states with no intermolecular stretching excitation.

The ground intermolecular state (K = 1/2) of o-H_2–OH is bound by ~47 cm^{-1}, in good accord with the experimentally determined value of 54 cm^{-1} [22]. The ground intermolecular state also has a relatively large parity splitting of 0.45 cm^{-1} for J = 1/2. Approximately 10 cm^{-1} higher in energy lies an excited intermolecular state (K = 1/2) with a parity splitting of 0.53 cm^{-1} for J = 1/2, but with opposite ordering of the parity levels. The energies and parity splittings calculated for these states are in very good agreement with the spectroscopic measurements presented in section 3 (see also table I of [26] for a more comprehensive comparison). We now examine

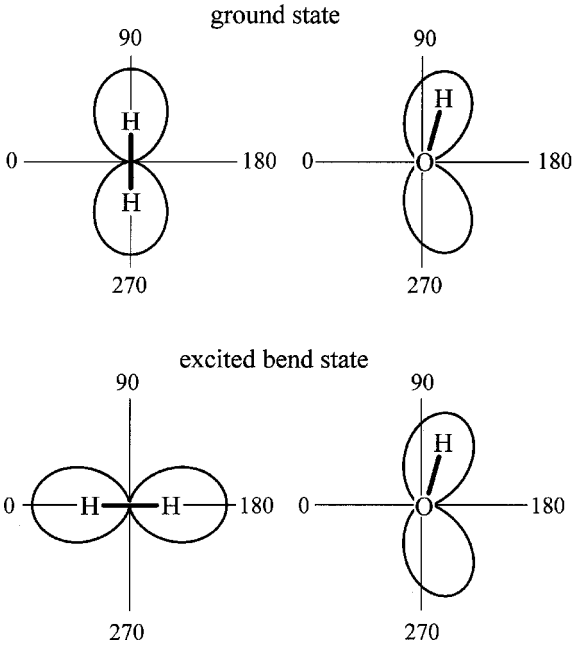

Figure 7. One-dimensional polar plots (in degrees) of the *o*-H_2 and OH angular probability distributions from quantum calculations on the MCKW *ab initio* potential [38]. The ground state of *o*-H_2–OH has its maximum probability amplitude at a near parallel configuration of the reactants, whereas the excited bend state has an L-shaped configuration that is reminiscent of the transition state to reaction. The relative orientation of the partners is well defined within the *o*-H_2–OH complex, and can be dramatically changed upon intermolecular bending excitation.

the nuclear wave functions associated with these two states in order to determine the degree of body-fixed orientation within the H_2–OH entrance channel complex.

4.3. *Wave functions*

The H_2–OH wave functions computed using a space-fixed representation [38] must be transformed into the body-fixed frame in order to explore the angular properties of the wave functions. The mathematical details of this transformation are given elsewhere [56, 80, 81]. The four-dimensional *o*-H_2–OH wave functions are used to construct one-dimensional polar plots of the H_2 and OH orientations with respect to the intermolecular axis by integrating over the remaining intermolecular coordinates. Polar plots of the angular probability distributions for the H_2 and OH monomers within the complex, $|\Psi|^2$ (θ_{H_2}) and $|\Psi|^2$ (θ_{OH}), are displayed adjacent to one another in figure 7. It should be noted that these distributions are indistinguishable for the two parity components of a given intermolecular state of *o*-H_2–OH; thus only the + parity component is shown in figure 7.

The angular probability distribution for the ground intermolecular state of *o*-H_2–OH is illustrated in the top part of figure 7. For this intermolecular state, the shape of the $|\Psi|^2$ (θ_{H_2}) distribution function reveals that the *o*-H_2 diatom is primarily in a $j_{H_2} = 1$ free rotor state with the H_2 molecule aligned perpendicular to the intermolecular axis ($\theta_{H_2} = 90°$ or 270°). Similarly, inspection of $|\Psi|^2$ (θ_{OH}) indicates that the OH diatom is also aligned nearly perpendicular to the intermolecular

axis (θ_{OH} = 115° or 245°), with the H end of OH pointing slightly away from the H_2 partner. From a classical perspective, H_2 is rotating in a helicopter type motion while OH precesses about the intermolecular axis with a large precessional angle. Therefore, the wave functions shown in figure 7 illustrate the remarkable conclusion that even though the two diatoms undergo nearly free internal rotation, they maintain a strong body-fixed alignment (H_2) and orientation (OH). The peak of the probability distribution for the ground state of *o*-H_2–OH occurs with the H_2 and OH diatoms in a near parallel configuration. This orientation is distinctly different from the T-shaped global minimum energy configuration on the V_{AVG} surface [38].

In contrast to the ground state, the angular probability distribution for the first excited intermolecular state of *o*-H_2–OH observed experimentally (lower portion of figure 7) shows that the *o*-H_2 diatom remains in a j_{H_2} = 1 free rotor state, but with the H_2 molecule aligned *along* the intermolecular axis (θ_{H_2} = 0° or 180°). In this case, the classical picture is that of H_2 undergoing a pinwheel rotational motion. From $|\Psi|^2$ (θ_{OH}), it is evident that in this particular excited bend state the OH angular distribution is unchanged from the ground state. The maximum in the probability distribution for *o*-H_2–OH in this excited intermolecular bend state occurs in an L-shaped configuration. This L-shaped configuration is reminiscent of the orientation of the diatoms at the transition state to reaction, although at a larger intermolecular distance [6].

In summary, the theoretically predicted wave functions for the bound states of *o*-H_2–OH have been explored in order to assess the relative orientation of the reactants in the intermolecular states observed experimentally. The angular probability distributions shown in figure 7 illustrate the relative orientation of the reactants in the lowest two intermolecular states of *o*-H_2–OH that have been observed, and demonstrate that the addition of one quantum of intermolecular bending excitation can dramatically change the relative orientation of the partners within the *o*-H_2–OH complex. This theoretical treatment enables us to assert that H_2–OH reactant complexes provide a new way to orient/ align reactants for stereodynamical studies, and that excitation of different intermolecular bend states will allow us to exert control over the initial configurations that are accessed in the dynamical studies.

5. Dynamics of vibrationally excited H_2–OH

The literature on the vibrational predissociation of weakly bound complexes is extensive, with insights into the nature of the dissociation process gained from a combination of experiment and theory [16, 17, 82]. For example, it has long been recognized that energy or momentum gap constraints are important in the dynamics [83, 84], the basic idea being that the final states that tend to be favoured are those with small translational energies. The rationale is that the overlap between the bound state wave function of the complex and the continuum wave function of the separated fragments will be best at low translational energies, since the continuum wave function becomes more oscillatory with increasing kinetic energy. Predissociation becomes more facile when a near resonant vibration-to-vibration (V–V) energy transfer pathway is available [84, 85, 86, 87], as a large fraction of the available energy is 'soaked up' in vibration(s) leaving little excess energy available for translation of the fragments. However, very little is known either experimentally or theoretically about the decay dynamics of weakly bound complexes on a *reactive* PES.

Vibrational predissociation of H_2–OH can proceed by different mechanisms depending on which partner is vibrationally excited. Excitation of the H_2 vibrational

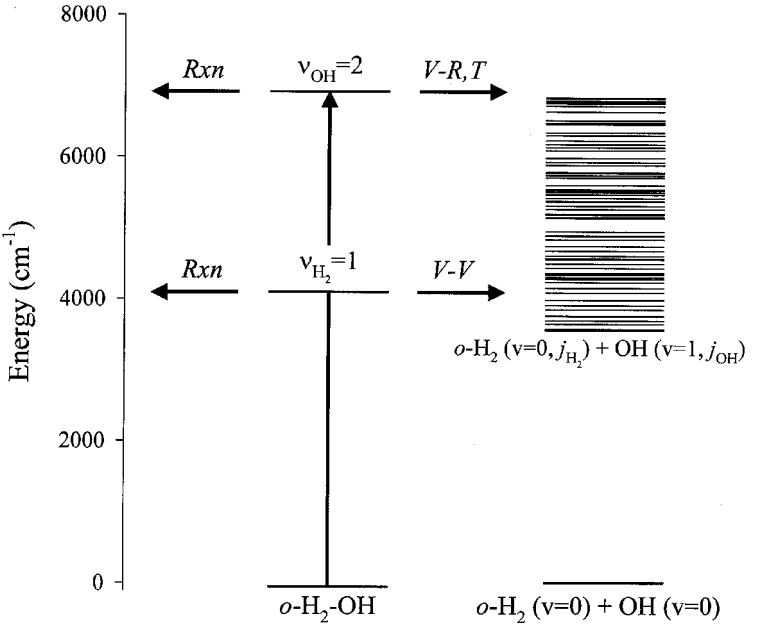

Figure 8. Energy diagram illustrating the intramolecular vibrational states of o-H_2–OH prepared by infrared overtone and stimulated Raman excitation relative to the o-H_2 + OH fragment rovibrational channels. The o-H_2–OH (v_{OH} = 2) complex predissociates by a vibration-to-rotation and/or translation (V–R,T) energy transfer process with a large energy gap ~3350 cm^{-1}. Predissociation of o-H_2–OH (v_{H_2} = 1) yields the same products, o-H_2 (v = 0, j_{H_2}) + OH (v = 1, j_{OH}), but by an efficient vibration-to-vibration (V–V) mechanism that leaves only 530 cm^{-1} of energy available to rotation and translation of the fragments. The vibrationally activated complexes can also decay by reaction (Rxn) to H_2O + H products.

mode allows for the possibility of vibrational predissociation by near resonant V–V energy transfer to the OH partner

$$H_2\text{–}OH(v_{H_2} = 1) \rightarrow H_2(v = 0,\ j_{H_2}) + OH(v = 1,\ j_{OH}) \quad (1)$$

with an exothermicity of ~529 cm^{-1}. On the other hand, in the case of OH vibrational overtone excitation, no near resonant V–V pathway is open and vibrational predissociation can only occur via a vibration-to-rotation and/or translation (V–R,T) energy transfer mechanism

$$H_2\text{–}OH(v_{OH} = 2) \rightarrow H_2(v = 0,\ j_{H_2}) + OH(v = 1,\ j_{OH}) \quad (2)$$

with an exothermicity of ~3350 cm^{-1}. Processes (1) and (2) are illustrated schematically in figure 8.

In addition to the vibrational predissociation processes that produce H_2 + OH fragments, there is also the possibility of reaction between the partners. Reaction can occur, even in the ground vibrational state, because the H_2–OH entrance channel complex lies above the H_2O + H asymptote. Moreover, vibrational excitation of the H_2 or OH partner provides enough energy to surmount the barrier to reaction, which can significantly increase the probability of reaction.

Excitation of different intramolecular vibrational modes of H_2–OH is expected

to have a pronounced effect on both the inelastic (vibrational predissociation) and reactive scattering dynamics. Our current experimental arrangement enables us to selectively excite either the $v_{H_2} = 1$ and $v_{OH} = 2$ vibrational states of H_2–OH and investigate the subsequent decay dynamics in the time and frequency domains. This is accomplished by monitoring the OH X $^2\Pi$ ($v = 1$) fragments resulting from the vibrational predissociation, process (1) or (2). The lifetime of vibrationally excited H_2–OH yields information regarding the combined rates of inelastic scattering and chemical reaction, since this is a unimolecular process with parallel decay channels. Only one of the decay channels, vibrational predissociation, has been observed to date, and thus we have not yet been able to determine the branching between the two decay channels or their relative rates of decay.

The mode-selective decay dynamics of vibrationally activated H_2–OH entrance channel complexes have also been the focus of recent theoretical studies [25, 29]. Unlike the experimental studies, reaction and vibrational predissociation can be treated separately in a theoretical calculation. Towards this end, time-dependent quantum wavepacket calculations have been performed on the vibrational predissociation dynamics of H_2–OH that neglect the possibility of reaction [25, 29]. The theory employed did not take into account the reactive channel in the expansion of the potential or the basis set for the quantum scattering calculations. Therefore, it will be informative to see if any inferences can be made about reactivity of vibrationally excited H_2–OH by comparing the experimental results with the theoretical calculations.

5.1. *Lifetime*

Time-resolved experiments involve varying the delay between the IR or SRE pump and UV probe pulses to obtain the rate of appearance of the OH ($v = 1$) fragments. The rate obtained is equal to the inverse lifetime of the vibrationally activated complex and reflects the *sum* of the rates for vibrational predissociation (VP) and reaction (Rxn). In the case of IR overtone excitation of *o*-H_2–OH, the IR pump laser was fixed on the $Q(1/2)^-$ transition of the pure overtone band located at 6972.3 cm^{-1} (marked with * in figure 4). Alternatively, in the case of SRE excitation of *o*-H_2–OH, the frequency difference between the PUMP and STOKES lasers was fixed on the centre of the *Q*-branch of the fundamental H_2 stretch shown in figure 4.

The time evolutions of the OH X $^2\Pi$ ($v = 1$, j_{OH}) fragments resulting from IR overtone excitation of OH and SRE of H_2 within the H_2–OH complex are shown in figure 9 [25, 27–29]. No OH A–X LIF signal is observed when the UV probe laser arrives in the interaction region prior to vibrational excitation of the complex. As the lasers become temporally overlapped, the LIF signal begins to rise and eventually reaches a maximum following a single exponential time profile. Also displayed in figure 9 are nonlinear least squares fits of the time profiles using a single exponential rise function with a unimolecular rate constant $k = 1/\tau$

$$S(\Delta t) = A[1 - \exp(-\Delta t/\tau)] \tag{3}$$

convoluted over a Gaussian excitation function. The lifetimes of the vibrationally excited *o*-H_2–OH complexes (table 1) were derived from this fitting procedure.

For *o*-H_2–OH prepared with two quanta of OH stretch, the lifetime is determined to be 115 ± 26 ns [25–27, 29]. By contrast, the lifetime of *o*-H_2–OH with one quantum of H_2 stretch is less than the instrumental time resolution of 7 ns [28, 29]. The more rapid decay can be attributed, at least in part, to the fact that a V–V process is

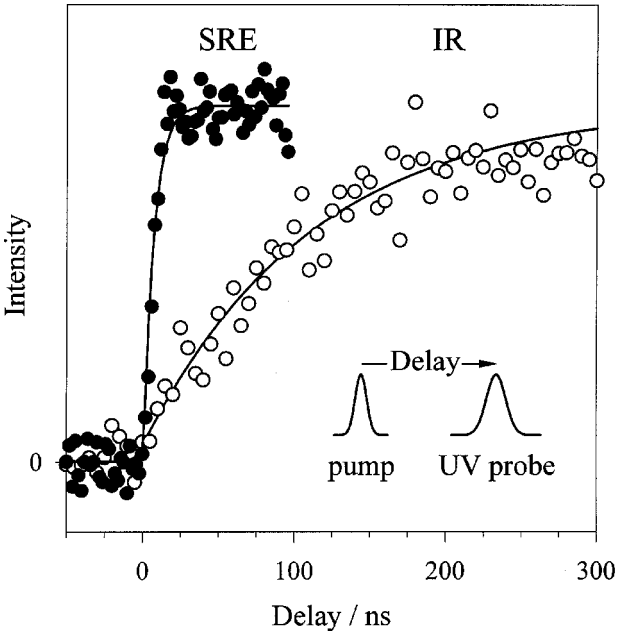

Figure 9. Time evolution of OH (v = 1) fragments arising from predissociation of vibrationally activated o-H_2–OH complexes, monitored by laser-induced fluorescence of OH A–X (0,1) transitions. The open circles are data obtained by monitoring OH fragments following infrared overtone excitation of o-H_2–OH to v_{OH} = 2. Fits to repeated scans of the OH risetime give an excited vibrational state lifetime of 115 ± 26 ns. In contrast, the rise of the OH signal following stimulated Raman excitation of o-H_2–OH to v_{H_2} = 1 is limited by the temporal resolution of the laser pulses (⩽7 ns). Figure adapted from [29].

Table 1. Lifetimes for o-H_2–OH with H_2 or OH vibrational excitation from experimental measurements, quantum calculations, and kinetic estimates.

o-H_2–OH	v_{H_2} = 1	v_{OH} = 2
Experimental lifetime[a]	7 ns	115 ± 26 ns
Vibrational predissociation lifetime [b]	22 ns	210 ns
Estimated unimolecular decay time [c]	~ 1 ns	⩾75 ns

[a] References [25–29].
[b] Time-dependent quantum wavepacket calculation of the vibrational predissociation lifetime [25, 29].
[c] Estimated from the bimolecular rate coefficients [60–62, 96] for removal of the vibrationally activated species through reaction and/or vibrational deactivation.

energetically possible for vibrational predissociation of H_2–OH (v_{H_2} = 1), while it is not open for H_2–OH (v_{OH} = 2). However, the enhanced reactivity of H_2 (v = 1) with OH (v = 0) as compared to H_2 (v = 0) with OH (v = 2) may also contribute to the significant change in lifetime.

The vibrational predissociation lifetimes derived from the quantum scattering calculations [25, 29] are compared with the measured lifetimes in table 1. Both experiment and theory show that the lifetime of vibrationally activated o-H_2–OH is highly dependent upon the intramolecular mode excited. The calculated lifetimes

for H_2 and OH intramolecular excitation are significantly different at 22 ns and 210 ns, respectively [25, 29]. As expected, the lifetime for o-H_2–OH ($v_{H_2} = 1$) is much shorter than that for o-H_2–OH ($v_{OH} = 2$) due to the facile V–V mechanism. This is similar to a recent comparison of the vibrational predissociation lifetimes for o-H_2–OH and p-D_2-OH prepared with two quanta of OH stretch, where the faster decay was attributed to a near resonant V–V pathway [25, 30].

The absolute agreement between experiment and theory for o-H_2–OH ($v_{OH} = 2$) is within a factor of two, which is quite promising given the sensitivity of the calculated lifetime to the potential [25, 29]. The close agreement also suggests that vibrational predissociation is likely to be the dominant decay channel for o-H_2–OH ($v_{OH} = 2$), since the calculations do not take the reactive channel into account. Similar quantitative accord between experiment and theory has also been observed for the vibrational predissociation of p-D_2–HF [74, 89].

It is informative to compare the degree of mode selectivity for the lifetimes measured experimentally with those predicted theoretically. The experimental observations reveal a more than 16-fold decrease in the lifetime of vibrationally activated o-H_2–OH when the initial excitation is placed in the H_2 mode as compared to the OH stretch. The theoretical calculations predict only a 10-fold change. One possible origin for this discrepancy is that the experimental lifetimes necessarily contain contributions from both vibrational predissociation *and* chemical reaction, while the theoretical calculations consider only vibrational predissociation. Thus, the enhanced mode selectivity seen experimentally could be a measure of the importance of the reactive decay channel. Vibrational excitation of the H_2 bond would be expected to have a pronounced effect on reactivity since it is strongly coupled to the reaction coordinate. A significant contribution from reaction, with a rate comparable to vibrational predissociation, would decrease the lifetime of H_2–OH ($v_{H_2} = 1$) and increase the degree of mode selectivity.

5.2. *Inelastic scattering dynamics*

Frequency-resolved experiments were also undertaken to probe the nascent OH product state distribution resulting from vibrational predissociation of the H_2–OH complex. In this instance, the UV probe laser was scanned through various OH A–X (0,1) rovibronic transitions [70], with the SRE or IR pump laser frequency and the time delay between the pump and probe lasers held fixed. The UV probe laser was also scanned across various OH A–X (1,0) transitions; however, no OH ($v = 0$) products were detected. The observation of OH ($v = 1$) products following excitation of the H_2 stretching mode confirms that vibrational predissociation proceeds via a V–V energy transfer mechanism, process (1). All experimental measurements of OH A–X transition intensities were performed in a fully saturated LIF regime and were appropriately converted into relative populations of the OH rotational levels [27, 90, 91].

The OH X $^2\Pi$ ($v = 1, j_{OH}$) product state distributions arising from vibrational predissociation of o-H_2–OH ($v_{H_2} = 1$) and ($v_{OH} = 2$) have been measured for each final OH rotor level j_{OH}. The relative populations of the rotor levels in the lower spin–orbit manifold of OH ($! = 3/2$), summed over λ-doublet components, are plotted in figure 10. The OH ($v = 1$) products are produced in rotational states with $j_{OH} \leqslant 11/2$ ($E_{rot} \sim 525\,cm^{-1}$) and $j_{OH} \leqslant 23/2$ ($E_{rot} \sim 2300\,cm^{-1}$) for H_2 and OH stretching excitation, respectively. In each case, the population in the lowest OH

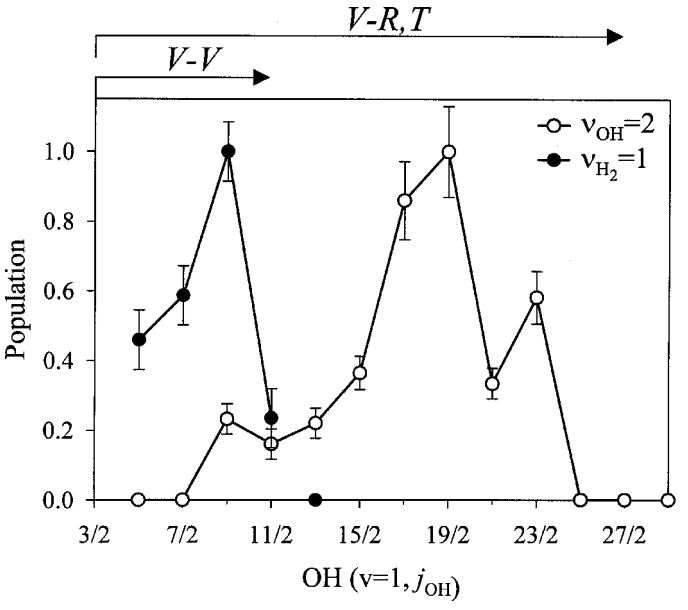

Figure 10. Experimental OH X $^2\Pi$ (v = 1, j_{OH}) product rotational state distributions following vibrational predissociation of the v_{H_2} = 1 (•) and v_{OH} = 2 (○) excited vibrational states of *o*-H_2–OH. The arrows on top indicate the j_{OH} rotational states that are energetically open for the V–V and V–R,T mechanisms. Figure adapted from [29].

rotational level (j_{OH} = 3/2) could not be probed due to interference from the large residual background population of this state within the supersonic expansion.

The total energy available for product rotational and translational excitation, 529 cm^{-1} or 3350 cm^{-1}, is readily evaluated from the SRE or IR transition frequency, the well known vibrational term values of H_2 and OH [69, 79], and the experimentally derived ground state binding energy D_0 = 54 cm^{-1} for *o*-H_2–OH [22]. Thus, it follows that OH rotor states with $j_{OH} \leqslant 11/2$ and $j_{OH} \leqslant 27/2$ are energetically accessible following vibrational predissociation of *o*-H_2–OH (v_{H_2} = 1) and (v_{OH} = 2), consistent with the experimental distributions shown in figure 10.

For *o*-H_2–OH (v_{H_2} = 1), the correlated *o*-H_2 partner is restricted to the j_{H_2} = 1 rotor state by energetic and kinetic considerations [28]. This assumes no interchange between *o*- and *p*-H_2 on the time scale of the experiment (100 ns). Thus, for process (1), correlated (j_{OH},j_{H_2}) fragment pairs can be designated unambiguously by probing only the OH fragment. It is noteworthy that the experimental population distribution peaks at (9/2, 1) rather than the near resonant (11/2, 1) channel, which would be favoured based on energy gap arguments [83, 84]. This observation may be understood in terms of the large classical impact parameter (6–10 Å) that would be required to generate enough torque on recoiling OH and H_2 fragments, given the low translational energy release for the (11/2, 1) pair of only 4 cm^{-1} [27, 28, 92]. This indicates that angular momentum places a constraint on the predissociation dynamics for the near resonant (11/2, 1) channel.

For *o*-H_2–OH (v_{OH} = 2) predissociation, the long lifetime and experimental product state distribution are consistent with a V–R,T mechanism that releases

$\sim$3350 cm^{-1} for rotational and translational excitation of the OH (v = 1) and o-H_2 (v = 0) fragments [27]. In this case, population in a given j_{OH} level may contain contributions from more than one pair of correlated (j_{OH},j_{H_2}) fragments. Within the assumption that translational energy will be minimized, however, we can identify the highest energetically allowed (j_{OH},j_{H_2}) pair associated with each of the OH product rotational channels. Those that minimize translational energy, namely (j_{OH},j_{H_2}) = (19/2, 5), (23/2, 3) and (17/2, 5), correspond to the most populated OH rotor levels in the predissociation process. A few (j_{OH},j_{H_2}) channels with either high OH or high H_2 rotational angular momentum are not observed, e.g. (25/2, 3), (27/2, 1), (5/2, 7) and (7/2, 7), presumably due to anisotropy constraints imposed by the intermolecular potential [27].

The inelastically scattered OH (v = 1, j_{OH}) fragments also exhibit significant fine structure effects that are discussed in detail elsewhere [27, 28, 30]. Here, we simply note that vibrational predissociation of o-H_2–OH (v_{H_2} = 1) and (v_{OH} = 2) yields OH fragments in both spin–orbit manifolds with nearly equal populations. Moreover, the OH fragments from o-H_2–OH (v_{OH} = 2) show a strong λ-doublet propensity in the lower spin–orbit manifold, which indicates that the OH unpaired $p\pi$ orbital is preferentially aligned perpendicular to the rotation plane of the OH products. The OH λ-doublet preferred in vibrational predissociation of o-H_2–OH, $\Pi(A'')$, is *opposite* to that seen in full collisions where the $\Pi(A')$ λ-doublet is generally favoured [55, 93, 94]. This change is attributed to the limited angular region of the V_{DIF} and V_{AVG} potentials accessed in the H_2–OH complex [27, 30]. Excitation of the H_2 mode in o-H_2–OH, however, does not yield a significant OH λ-doublet preference, and the reason for this change is not known [28].

5.3. *Comparison with full collisions*

Previous kinetic studies have determined the rate coefficients for reaction and/or vibrational deactivation in full collisions between OH (v = 0) + H_2 (v = 1) and OH (v = 2) + H_2 (v = 0) at 298 K [60–62, 94–96]. It is informative to compare the bimolecular rate constants obtained from the collision studies with the unimolecular decay rates measured for vibrationally activated H_2–OH (v_{H_2} = 1 and v_{OH} = 2). This comparison may reveal changes in the decay dynamics between full collisions, which sample all possible orientations of the reactants, and half-collisions that are initiated from a restricted range of configurations imposed by the entrance channel complex (figure 7).

The rate constant for total loss of OH (v = 0) in collisions H_2 (v = 1), k_{01} (298 K) = 7.5×10^{-13} cm^3 molecule^{-1} s^{-1}, was obtained by monitoring OH (v = 0) as a function of time in a flow tube apparatus [61, 62, 95, 96]. These studies attributed the measured rate constant (k_{01}) to reaction, after considering the possible effect of non-reactive V–V energy transfer on the interpretation of their results. The rate coefficient for total removal of OH (v = 2) in collisions with H_2 (v = 0), k_{20} (298 K), was determined to be less than 10^{-14} cm^3 molecule^{-1} s^{-1} [60, 88]. In this case, the loss of OH (v = 2) has been attributed primarily to vibrational relaxation and not reaction. For reference, the recommended value of the rate coefficient for the OH (v = 0) + H_2 (v = 0) reaction is k_{00} (298 K) = 6.7×10^{-15} cm^3 molecule^{-1} s^{-1} [97].

In order to compare the unimolecular decay rates for vibrationally excited H_2–OH with collisional studies, the bimolecular rate coefficient must first be converted into a reaction probability by relating the experimentally determined rate coefficient to the purely gas kinetic collision rate coefficient [98]. The overall removal rate

coefficient for H_2 (v = 0) + OH (v = 2) leads to a total removal probability of $< 2.0 \times 10^{-5}$ per gas kinetic collision. Similarly, the overall rate coefficient for the H_2 (v = 1) + OH (v = 0) reaction leads to a total removal probability of 1.8×10^{-3}. Next, an estimate of the collision rate in the complex is required to relate the total removal probability to the unimolecular decay rate measured for vibrationally excited H_2–OH in the present studies. The collision rate in the H_2–OH complex will correspond to the frequency associated with the zero point vibrational motion of the intermolecular stretching coordinate, which is anticipated to be on the order of 25 cm^{-1}, based on *ab initio* quantum calculations [38]. Combining this total removal probability and collision rate yields an estimate of >75 ns for the lifetime of the *o*-H_2–OH (v_{OH} = 2) complex and ~1 ns for the *o*-H_2–OH (v_{H_2} = 1) complex (table 1). Based on the full collision studies, these estimated decay times would be associated primarily with vibrational relaxation for v_{OH} = 2 and chemical reaction for v_{H_2} = 1.

The experimentally determined lifetimes of 115 ns and <7 ns for the vibrationally excited complexes, *o*-H_2–OH (v_{OH} = 2) and *o*-H_2–OH (v_{H_2} = 1), are in remarkably close agreement with the lifetimes estimated using the bimolecular rate coefficients. Based strictly on this comparison with kinetic rate measurements, one might infer that reaction may also be taking place in *o*-H_2–OH (v_{H_2} = 1). However, such an argument does not take into account the restricted range of initial orientations sampled in the *o*-H_2–OH complex. In a previous report, we presumed that the configuration of the reactants in the ground intermolecular state of *o*-H_2–OH was the T-shaped OH–H_2 structure at the minimum of the potential well [28], which is not directly amenable to reaction. The plot of the angular probability distributions for *o*-H_2–OH (figure 7), however, reveals that OH is indeed suitably oriented for reaction in the ground and excited bend states [6]. In addition, the H_2 partner needs to be aligned nearly along the intermolecular axis (HHO angle of 162°) to reach the transition state geometry [6]. Both the ground and excited bend states of *o*-H_2–OH access this configuration (figure 7), albeit with greater probability amplitude for the excited bend, and therefore both initial states should be amenable to reaction.

6. Implications for reaction

In this section, we examine the location of the H_2–OH entrance channel complex on the reactive potential surface and consider the likelihood for reaction upon vibrational activation of *o*-H_2–OH. The six-dimensional PES for the OH + H_2 → H_2O + H reaction is shown as a contour diagram of reduced dimensionality in figure 11. This potential is the reactive (A′) surface developed recently by Ochoa de Aspuru and Clary [48]. The relative orientation between the OH and H_2 reactants in the entrance channel is fixed at the transition state structure (see figure 11), and the H_2O + H products maintain this same configuration in the exit channel. Given this constraint, the entrance channel can be depicted as the centre-of-mass separation of the OH and H_2 reactants R, while the exit channel is plotted as a function of the intramolecular H_2 bond length r_{H_2}. The OH bond length r_{OH} is essentially unchanged in evolving from the OH reactant to the H_2O product, and is not shown in figure 11. Thus, there are primarily two motions that transform OH + H_2 reactants into H_2O + H products: shortening the intermolecular separation distance R and elongating the H_2 bond r_{H_2}.

The *o*-H_2–OH wave functions derived from the MCKW *ab initio* potential (section 4) can now be projected onto the reactive PES. This is achieved by plotting the *o*-H_2–OH probability amplitude in the two-dimensional representation, r_{H_2} versus

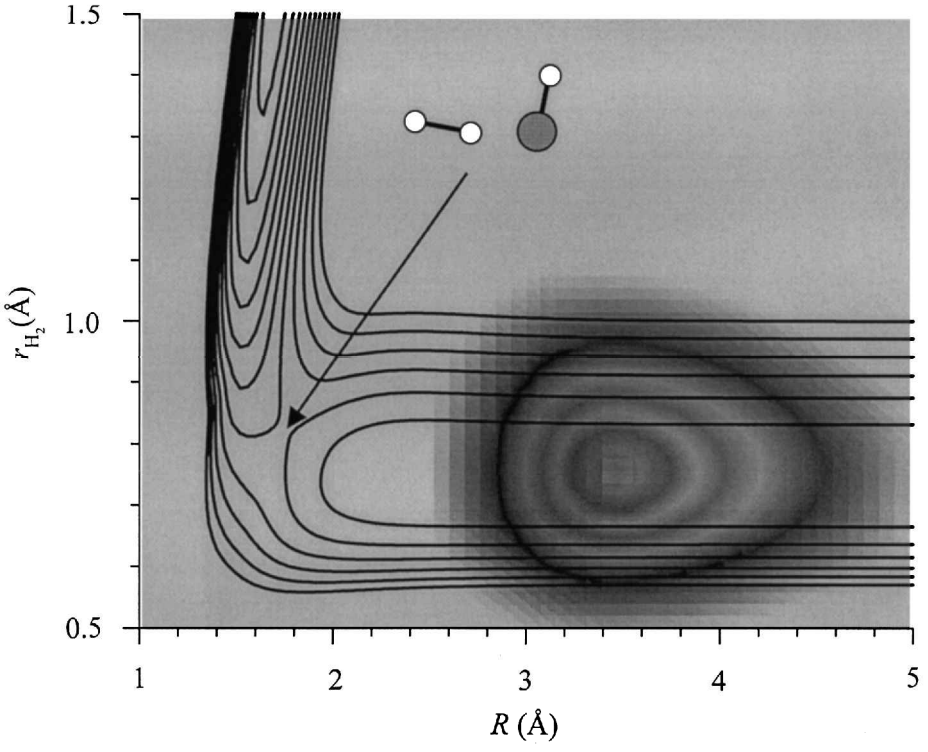

Figure 11. Probability distribution of o-H_2–OH entrance channel complex superimposed on the reactive OH + H_2 → H_2O + H potential energy surface [48]. The entrance channel is represented by the intermolecular separation of the reactants R and the exit channel is plotted as the intramolecular H_2 bond length r_{H_2}. The relative orientation of the reactants/ products is fixed at the transition state structure (inset). The potential energy contours are drawn in steps of 1000 cm^{-1} from −4000 cm^{-1} to 6000 cm^{-1}, while the probability distribution is depicted with a grey scale that spans three orders of magnitude.

R, of the reactive PES. (The H_2 stretching potential in o-H_2–OH is assumed to be the same as the H_2 monomer.) Since the orientation of the OH + H_2 reactants is constrained to the transition state structure in drawing the potential energy contours (figure 11), this same restriction has been applied to the o-H_2–OH wave functions. The probability density distribution for the ground intermolecular state of o-H_2–OH is displayed in figure 11. The probability amplitude is illustrated using a grey scale that ranges over three orders of magnitude. The o-H_2–OH probability distribution is peaked in the entrance channel at R = 3.5 Å. The spread of the probability distribution along the R axis represents the zero-point intermolecular stretching motion of o-H_2–OH, while the spread along r_{H_2} corresponds to the zero-point H_2 stretching motion.

By stabilizing the o-H_2–OH reactant complex, the reactants have been localized in the entrance channel and are poised for reaction. Infrared or stimulated Raman excitation of the OH or H_2 modes of o-H_2–OH will promote the wavepacket to energies above the barrier to reaction with the spectroscopic transition moment driving the wavepacket along the OH or H_2 coordinate, respectively. Clearly, the

possibility of reaction is expected to be greater when exciting the H_2 reactive mode than the OH spectator mode. Furthermore, intermolecular excitation can be used to manipulate the relative orientation of the partners within the *o*-H_2–OH complex, in some cases accessing configurations that are even more favourable for reaction.

The *ab initio* surface in figure 11 represents the electronic potential energy as a function of the nuclear coordinates of the four atoms. For vibrationally mediated reactions, the effective potential for reaction, typically denoted as vibrationally adiabatic potential curves [63, 66], can be substantially different than the minimum energy path along the *ab initio* surface. Theoretical analyses of the OH + H_2 reaction have shown that the effective height, shape and location of the barrier to reaction changes substantially upon vibrational excitation of H_2 as compared to that for ground state reagents [42, 63, 66]. Specifically, the calculations of Truong reveal that the barrier falls from 2300 cm^{-1} for OH (v = 0) + H_2 (v = 0) to 1400 cm^{-1} for H_2 (v = 1) [66]. In addition, the transition state moves into the entrance channel by about 0.3 Å when H_2 is vibrationally excited. One possible interpretation of these calculations is that the transition state occupies a greater region of configuration space for the OH (v = 0) + H_2 (v = 1) reaction, thereby relaxing some of the geometrical constraints placed on the ground state reaction. This may, in turn, enhance the probability of reactive decay for *o*-H_2–OH (v_{H_2} = 1).

The question that still remains is to what extent reaction contributes to the decay dynamics of vibrationally activated *o*-H_2–OH. Of course, the ideal way to answer this question definitively is to detect the H or H_2O reaction products directly. Such experiments are currently underway in this laboratory. These experiments are quite challenging because these very same products are formed in the course of synthesizing H_2–OH complexes in the supersonic expansion, and they create a significant background signal when probing the H-atom products [99].

The possibility of inducing reaction by vibrational activation of weakly bound complexes has been considered in several theoretical studies. In 1986, Pollak and Naaman suggested that vibrational excitation of van der Waals molecules could lead to chemical reaction instead of vibrational predissociation, and they termed the former process vibrational pre-reaction [100]. Schinke and co-workers later explored a mechanism for vibrational pre-reaction based on tunnelling of a light atom using a collinear atom–diatom model [101]. More recently, Paniagua *et al.* have carried out time-dependent wavepacket calculations to evaluate the reaction probability upon infrared excitation of Li–HF van der Waals precursors [102, 103]. They find a high probability (>90%) of forming LiF products for HF Δv = 1 and 2 transitions of Li–HF. Similarly, Takayanagi and Kurosaki have investigated the pre-reaction process in the H–HF van der Waals molecule upon HF vibrational excitation [104]. They observe resonances associated with H–HF (v = 3,j) that evolve into F + H_2 products by tunnelling through the barrier, albeit with a much smaller probability than predissociation into H + HF. Analogous calculations would certainly be valuable in evaluating the likelihood of reaction for *o*-H_2–OH (v_{H_2} = 1). Of course, this requires a global potential energy surface for OH + H_2 that is accurate in both the entrance channel and transition state regions.

Before closing, we note that Johnson and co-workers have recently succeeded in detecting reaction products following vibrational activation of $Cl^-{\cdot}CH_3Br$ entrance channel complexes [105]. They have activated the C–H stretching mode of $Cl^-{\cdot}CH_3Br$ and detected the Br^- product of the S_N2 reaction. Here, the transition state lies below the energy of reactants, so that excitation of the C–H stretching

mode can initiate reaction, but not vibrational predissociation of the $Cl^-\cdot CH_3Br$ complex. In this system, the long-range ion–dipole forces orient the reactants in a C_{3v} structure that is conducive to reaction with the chloride ion bound to the hydrogens of the methyl pocket.

7. Conclusions

Weakly bound complexes composed of the OH and H_2 reactants have been stabilized in the entrance channel to the OH + H_2 → H_2O + H reaction, and probed by infrared and stimulated Raman excitation of the high frequency OH and H_2 intramolecular modes of H_2–OH. In addition, the low frequency intermolecular modes have been observed as combination bands built on the high frequency OH vibrational transition. These intermolecular vibrations reflect the angular and radial properties of the attractive multipolar interactions between the OH and H_2 reactants in the entrance channel to reaction. Comparisons between experimental measurements and theoretical calculations of the energies for the intermolecular states enable the topology of various OH + H_2 potentials to be evaluated and ultimately refined. Such a comparison has shown that the MCKW *ab initio* potential provides a reliable description of the OH + H_2 interaction in the entrance channel to reaction.

The long-range forces that bind the OH and H_2 reactants together also restrict the range of orientations sampled by the partners in the entrance channel complexes. Theoretical calculations based on the MCKW potential predict that the OH (j_{OH} = 3/2) and *o*-H_2 (j_{H_2} = 1) reactants have a remarkably well-defined spatial orientation in the body-fixed frame of the complex. Furthermore, the relative orientation of the OH and H_2 partners is found to be dramatically different for various intermolecular bend states of *o*-H_2–OH. Specifically, the ground intermolecular state has a near parallel configuration of the diatoms, while an excited bend state favours an L-shaped configuration that is reminiscent of the transition state to reaction. As a result, intermolecular excitation can be used to manipulate the relative orientation of the reactants within the *o*-H_2–OH complex for stereodynamic studies.

Vibrational activation of the H_2–OH entrance channel complexes also induces reactive and/or inelastic scattering dynamics between the partners. Direct time-domain lifetime measurements have demonstrated a pronounced change in the lifetime of vibrationally activated H_2–OH, depending on whether the H_2 or OH mode is excited. This mode selectivity is attributed, at least in part, to an open vibrational-to-vibration energy transfer channel for H_2–OH (v_{H_2} = 1) that is closed for H_2–OH (v_{OH} = 2), although enhancement in the rate of reaction upon H_2 vibrational excitation may also contribute to the change in lifetime. Time-dependent quantum wavepacket calculations and kinetic estimates based on bimolecular rate coefficients leave open the possibility that reaction plays a role to the rapid decay of H_2–OH (v_{H_2} = 1). The challenge for the future is to assess the branching fractions for reaction and vibrational predissociation following state specific vibrational excitation of H_2–OH.

Acknowledgments

The authors would like to acknowledge the valuable contributions of Michael W. Todd, Rebecca L. Schwartz and Jeanne M. Hossenlopp (Marquette University) to the experimental work described in this review article. We also wish to thank Paul J. Krause, Steven M. Miller and David C. Clary (University College, London)

for insightful discussions, carrying out complementary theoretical calculations on H_2–OH, and supplying us with their 4D bound state code. This research has been supported by grants from the Chemistry Division of the National Science Foundation and the Office of Basic Energy Sciences of the Department of Energy. Acknowledgment is also made to the donors of the Petroleum Research Foundation, administered by the ACS, for partial support of this research.

References

[1] Manolopoulos, D., 1997, *J. chem. Soc. Faraday Trans*., **93,** 673.
[2] Skodje, R. T., Skouteris, D., Manolopoulos, D. E., Lee, S.-H., Dong, F., and Liu, K., 2000, *J. chem. Phys*., **112,** 4536.
[3] Simpson, W. R., Rakitzis, T. P., Kandel, S. A., Levon, T., and Zare, R. N.,1996, *J. phys. Chem*., **100,** 7938.
[4] Orr-Ewing, A. J., Simpson, W. R., Rakitzis, T. P., Kandel, S. A., and Zare, R. N., 1997, *J. chem. Phys*., **106,** 5961.
[5] Alagia, M., Balucani, N., Casavecchia, P., Stranges, D., and Volpi, G. G., 1993, *J. chem. Phys*., **98,** 2459.
[6] Alagia, M., Balucani, N., Casavecchia, P., Stranges, D., Volpi, G. G., Clary, D. C., Kliesch, A., and Werner, H.-J., 1996, *Chem. Phys*., **207,** 389.
[7] Clary, D. C., 1998, *Science*, **279,** 1879.
[8] Zare, R. N., 1998, *Science*, **279,** 1875.
[9] Manolopoulos, D. E., Stark, K., Werner, H.-J., Arnold, D. W., Bradforth, S. E., and Neumark, D. M., 1993, *Science*, **262,** 1852.
[10] Bradforth, S. E., Arnold, D. W., Neumark, D. M., and Manolopoulos, D. E., 1993, *J. chem. Phys*., **99,** 6345.
[11] Neumark, D. M., 1993, *Acc. chem. Res*., **26,** 33.
[12] De Beer, E., Kim, E. H., Neumark, D. M., Gunion, R. F., and Lineberger, W. C., 1995, *J. phys. Chem*., **99,** 13627.
[13] Orr-Ewing, A. J., 1996, *J. chem. Soc. Faraday Trans*., **92,** 881.
[14] Skouteris, D., Manolopoulos, D. E., Bian, W., Werner, H.-J., Lai, L.-H., and Liu, K., 1999, *Science*, **286,** 1713.
[15] Meuwly, M., and Hutson, J. M., 2000, *J. chem. Phys*., **112,** 592.
[16] Nesbitt, D. J., 1988, *Chem. Rev*., **88,** 843.
[17] Miller, R. E., 1988, *Science*, **240,** 447.
[18] Heaven, M. C., 1992, *Ann. Rev. Phys. Chem*., **43,** 283.
[19] Lee, H.-S., McCoy, A. B., Harding, L. B., Carter, C. C., and Miller, T. A., 1999, *J. chem. Phys*., **111,** 10053.
[20] Bonn, R. T., Wheeler, M. D., and Lester, M. I., 2000, *J. chem. Phys*., **112,** 4942.
[21] Loomis, R. A., and Lester, M. I., 1995, *J. chem. Phys*., **103,** 4371.
[22] Loomis, R. A., Schwartz, R. L., and Lester, M. I., 1996, *J. chem. Phys*., **104,** 6984.
[23] Loomis, R. A., and Lester, M. I., 1997, *Ann. Rev. Phys. Chem*., **48,** 643.
[24] Schwartz, R. L., Anderson, D. T., Todd, M. W., and Lester, M. I., 1997, *Chem. Phys. Lett*., **273,** 18.
[25] Krause, P. J., Clary, D. C., Anderson, D. T., Todd, M. W., Schwartz, R. L., and Lester, M. I., 1998, *Chem. Phys. Lett*., **294,** 518.
[26] Anderson, D. T., Schwartz, R. L., Todd, M. W., and Lester, M. I., 1998, *J. chem. Phys*., **109,** 3461.
[27] Hossenlopp, J., Anderson, D. T., Todd, M. W., and Lester, M. I., 1998, *J. chem. Phys*., **109,** 10707.
[28] Wheeler, M. D., Todd, M. W., Anderson, D. T., and Lester, M. I., 1999, *J. chem. Phys*., **110,** 6732.
[29] Wheeler, M. D., Anderson, D. T., Todd, M. W., Lester, M. I., Krause, P. J., and Clary, D. C., 1999, *Molec. Phys*., **97,** 151.
[30] Todd, M. W., Anderson, D. T., and Lester, M. I., 2000, *J. phys. Chem.* A, **104**, 6532.
[31] Tsiouris, M., Wheeler, M. D., and Lester, M. I., 1999, *Chem. Phys. Lett*., **302,** 192.
[32] Wheeler, M. D., Tsiouris, M., Lester, M. I., and Lendvay, G., 2000, *J. chem. Phys*., **112**, 6590.

[33] Chen, Y., and Heaven, M. C., 1998, *J. chem. Phys.*, **109,** 5171.
[34] Liu, K., Kolessov, A., Partin, J. W., Bezel, I., and Wittig, C., 1999, *Chem. Phys. Lett.*, **299,** 374.
[35] Clary, D. C., 1994, *J. phys. Chem.*, **98,** 10678.
[36] Glassman, I., 1996, *Combustion* (San Diego: Academic Press).
[37] Millar, T. J., and Williams, D. A. (eds), 1988, *Rate Coefficients in Astrochemistry* (Dordrecht: Kluwer Academic Publ.).
[38] Miller, S. M., Clary, D. C., Kliesch, A., and Werner, H.-J., 1994, *Molec. Phys.*, **83,** 405.
[39] Ravishankara, A. R., Nicovich, J. M., Thompson, R. L., and Tully, F. P., 1981, *J. phys. Chem.*, **85,** 2498.
[40] Walch, S. P., and Dunning Jr, T. H., 1980, *J. chem. Phys.*, **72,** 1303.
[41] Schatz, G. C., and Elgersma, H., 1980, *Chem. Phys. Lett.*, **73,** 21.
[42] Schatz, G. C., 1981, *J. chem. Phys.*, **74,** 1133.
[43] Dunning Jr, T. H., Harding, L. B., Wagner, A. F., Schatz, G. C., and Bowman, J. M., 1988, *Science*, **240,** 453.
[44] Zhang, D. H., and Zhang, J. Z. H., 1994, *J. chem. Phys.*, **101,** 1146.
[45] Neuhauser, D., 1994, *J. chem. Phys.*, **100,** 9272.
[46] Manthe, U., Seideman, T., and Miller, W. H., 1994, *J. chem. Phys.*, **101,** 4759.
[47] Isaacson, A. D., 1997, *J. chem. Phys.*, **107,** 3832.
[48] Ochoa De Aspuru, G., and Clary, D. C., 1998, *J. phys. Chem.* A, **102,** 9631.
[49] Kochanski, E., and Flower, D. R., 1981, *Chem. Phys.*, **57,** 217.
[50] Offer, A. R., and Van Hemert, M. C., 1993, *J. chem. Phys.*, **99,** 3836.
[51] Schinke, R., and Andresen, P., 1984, *J. chem. Phys.*, **81,** 5644.
[52] Dewangan, D. P., Flower, D. R., and Danby, G., 1986, *J. Phys.* B: *At. molec. Phys.*, **19,** L747.
[53] Corey, G. C., and Alexander, M. H., 1988, *J. chem. Phys.*, **88,** 6931.
[54] Offer, A. R., Van Hemert, M. C., and Van Dishoeck, E. F., 1994, *J. chem. Phys.*, **100,** 362.
[55] Schreel, K., and Ter Meulen, J. J., 1996, *J. chem. Phys.*, **105,** 4522.
[56] Miller, S. M., and Clary, D. C., 1993, *J. chem. Phys.*, **98,** 1843.
[57] Ochoa De Aspuru, G., and Clary, D. C., 2000, private communication.
[58] Brouard, M., Burak, I., Markillie, G. A. J., McGrath, K., and Vallance, C., 1997, *Chem. Phys. Lett.*, **281,** 97.
[59] Hawthorne, G., Sharkey, P., and Smith, I. W. M., 1998, *J. chem. Phys.*, **108,** 4693.
[60] Spencer, J. E., Endo, H., and Glass, G. P., 1976, *Sixteenth Symposium (International) on Combustion* (Pittsburgh: The Combustion Institute), p. 829.
[61] Zellner, R., and Steinert, W., 1981, *Chem. Phys. Lett.*, **81,** 568.
[62] Glass, G. P., and Chaturvedi, B. K., 1981, *J. chem. Phys.*, **75,** 2749.
[63] Truhlar, D. G., and Isaacson, A. D., 1982, *J. chem. Phys.*, **77,** 3516.
[64] Zhang, D. H., and Zhang, J. Z. H., 1993, *J. chem. Phys.*, **99,** 5615.
[65] Zhang, D. H., and Zhang, J. Z. H., 1994, *J. chem. Phys.*, **100,** 2697.
[66] Truong, T. N., 1995, *J. chem. Phys.*, **102,** 5335.
[67] Clary, D. C., 1992, *J. chem. Phys.*, **96,** 3656.
[68] Viers, D. K., and Rosenblatt, G. M., 1987, *J. molec. Spectrosc.*, **121,** 401.
[69] Coxon, J. A., 1980, *Can. J. Phys.*, **58,** 933.
[70] Dieke, G. H., and Crosswhite, H. M., 1962, *J. quantum Spectrosc. Radiat. Transfer*, **2,** 97.
[71] Hartland, G. V., Henson, B. F., Venturo, V. A., Hertz, R. A., and Felker, P. M., 1990, *J. opt. Soc. Am.* B, **7,** 1950.
[72] Zwier, T. S., 1996, *Ann. Rev. Phys. Chem.*, **47,** 205.
[73] Lovejoy, C. M., Nelson Jr, D. D., and Nesbitt, D. J., 1987, *J. chem. Phys.*, **87,** 5621.
[74] Lovejoy, C. M., Nelson Jr, D. D., and Nesbitt, D. J., 1988, *J. chem. Phys.*, **89,** 7180.
[75] Herzberg, G., 1945, *Molecular Spectra and Molecular Structure 2. Infrared and Raman Spectra of Polyatomic Molecules* (New York: Van Nostrand Reinhold).
[76] Long, D. A., 1977, *Raman Spectroscopy* (New York: McGraw-Hill).
[77] Schwartz, C., and Le Roy, R. J., 1987, *J. molec. Spectrosc.*, **121,** 420.
[78] Felker, P. M., Maxton, P. M., and Schaeffer, M. W., 1994, *Chem. Rev.*, **94,** 1787.

[79] BRANNON, P. J., CHURCH, C. H., and PETERS, C. W., 1968, *J. molec. Spectrosc.*, **27,** 44.
[80] ANDERSON, D. T., and LESTER, M. I., 2000, in preparation.
[81] LAUNAY, J. M., 1977, *J. Phys.* B, **10,** 3665.
[82] LESTER, M. I., 1996, *Adv. Chem. Phys.*, **96,** 51.
[83] BESWICK, J. A., and JORTNER, J., 1981, *Adv. Chem. Phys.*, **47,** 363.
[84] EWING, G. E., 1979, *J. chem. Phys.*, **71,** 3143.
[85] EWING, G. E., 1980, *J. chem. Phys.*, **72,** 2096.
[86] EWING, G. E., 1982, *Faraday Discuss. Chem. Soc.*, **73,** 325.
[87] EWING, G. E., 1987, *J. phys. Chem.*, **91,** 4662.
[88] RENSBERGER, K. J., JEFFRIES, J. B., and CROSLEY, D. R., 1989, *J. chem. Phys.*, **90,** 2174.
[89] KRAUSE, P. J., and CLARY, D. C., 1998, *Molec. Phys.*, **93,** 619.
[90] ALTKORN, R., and ZARE, R. N., 1984, *Ann. Rev. Phys. Chem.*, **35,** 265.
[91] GUYER, D. R., HÜWEL, L., and LEONE, S. R., 1983, *J. chem. Phys.*, **79,** 1259.
[92] BRECKENRIDGE, W. H., JOUVET, C., and SOEP, B., 1986, *J. chem. Phys.*, **84,** 1443.
[93] ANDRESEN, P., HÄUSLER, H., and LÜLF, H. W., 1984, *J. chem. Phys.*, **81,** 571.
[94] ANDRESEN, P., ARISTOV, N., BEUSHAUSEN, V., HÄUSLER, D., and LÜLF, H. W., 1991, *J. chem. Phys.*, **95,** 5763.
[95] LIGHT, G. C., and MATSUMOTO, J. H., 1978, *Chem. Phys. Lett.*, **58,** 578.
[96] GERSHENZON, Y. M., DYUBKO, S. F., IVANOV, A. V., ILIN, S. D., KUCHERYAVYI, S. I., and ROZENSHTEIN, V. B., 1987, *High energy Chem.*, **21,** 403.
[97] DEMORE, W. B., SANDER, S. P., GOLDEN, D. M., HAMPSON, R. F., KURYLO, M. J., HOWARD, C. J., RAVISHANKARA, A. R., KOLB, C. E., and MOLINA, M. J., 1994, *Chemical Kinetics and Photochemical Data for use in Stratospheric Modeling* (Pasedena: Jet Propulsion Laboratory, California Institute of Technology).
[98] STEINFELD, J. I., FRANCISCO, J. S., and HASE, W. L., 1999, *Chemical Kinetics and Dynamics*, 2nd Edn (Englewood Cliffs, New Jersey: Prentice Hall, Inc.).
[99] ANDERSON, D. T., TODD, M. W., and LESTER, M. I., 1999, *J. chem. Phys.*, **110,** 11117.
[100] POLLAK, E., and NAAMAN, R., 1986, *Chem. Phys. Lett.*, **123,** 352.
[101] ENGEL, V., SCHINKE, R., and POLLAK, E., 1987, *J. chem. Phys.*, **87,** 1596.
[102] PANIAGUA, M., AGUADO, A., LARA, M., and RONCERO, O., 1998, *J. chem. Phys.*, **109,** 2971.
[103] PANIAGUA, M., AGUADO, A., LARA, M., and RONCERO, O., 1999, *J. chem. Phys.*, **111,** 6712.
[104] TAKAYANAGI, T., and KUROSAKI, Y., 1999, *Phys. Chem. Chem. Phys.*, **1,** 1099.
[105] AYOTTE, P., KIM, J., KELLEY, J. A., NIELSEN, S. B., and JOHNSON, M. A., 1999, *J. Am. chem. Soc.*, **121,** 6950.